

Detecting quasar bubbles in a CMB map with matched filtering

2 April 2023

ABSTRACT

XYZ

Key words: Cosmology - cosmic background radiation; Cosmology - theory

1 INTRODUCTION

2 THEORY OF MATCHED FILTERING

Matched filters are used to extract a desired signal from data which in our case are a set of sky maps at different frequencies. This is done by incorporating apriori knowledge of the spectral and spatial characteristics of the desired signal, to maximize the signal-to-noise (SNR) ratio of that desired signal in the unknown data. Matched filters have been extensively used to detect galaxy clusters through their thermal SZ signature since their introduction 20 years ago (Haehnelt & Tegmark 1996; Herranz et al. 2002; Melin et al. 2006) for the construction of cluster catalogs (Vanderlinde et al. 2010; Planck Collaboration et al. 2014, 2016; Melin, J.-B. et al. 2021; Zubeldia et al. 2021). In case of thermal SZ, both the spectral and spatial information of the desired object can be utilized in the matched filtering approach.

A general matched filter, is hence, defined as the following in Fourier space (Melin et al. 2005, 2006):

$$\Psi_{\theta_c}(\mathbf{k}) = \sigma_{\theta_c}^2 \mathbf{P}^{-1}(\mathbf{k}) \mathbf{F}_{\theta_c}(\mathbf{k}), \quad (1)$$

where $\Psi_{\theta_c}(\mathbf{k})$ is a filter with frequency index i and,

$$\sigma_{\theta_c} = \left[\int d^2k \mathbf{F}_{\theta_c}^t(\mathbf{k}) \cdot \mathbf{P}^{-1}(\mathbf{k}) \cdot \mathbf{F}_{\theta_c}(\mathbf{k}) \right]^{-1/2}. \quad (2)$$

In the flat sky approximation, which we use here, the fourier mode is related to angular multipole, $\ell = 2\pi k$. The beam smoothed source profile function $\mathbf{F}_{\theta_c}(\mathbf{k}) = \mathbf{B}_{\theta_c}(\mathbf{k}) \cdot \mathbf{X}_{\theta_c}(\mathbf{k})$, where $\mathbf{B}_{\theta_c}(\mathbf{k})$ is the beam in Fourier-space, $\mathbf{X}_{\theta_c}(\mathbf{k})$ is the assumed source profile in Fourier-space. $\mathbf{P}(\mathbf{k})$ is the noise covariance, which is essentially all foreground components (CMB, kSZ, IR sources, Radio sources, instrumental noise etc.) except the component that we want to detect through the matched filter. Typically the filter is function of size of the desired object and also depend upon angular location of that object in the map. Applying this filter on an input map (i.e., a real space convolution of the matched filter and the input map) gives us an estimate of the amplitude of the desired signal at a given location in the map. To get SNR, we just divide the matched filtered map by σ_{θ_c} which can be thought of as a noise estimate due to all non-desirable signal sources.

An important thing to note is that this simple matched filter is usually applied to datasets with Gaussian noise, since it is optimal for those cases. While Gaussianity is not a requirement, this matched filter may no longer be optimal in the presence of non-Gaussian noise (Melin et al. 2006). Optimal matched filters for low number count

Poisson noise, however, have been derived for use in X-ray and γ -ray observations (Ofek & Zackay 2018; Vio & Andreani 2018).

In this paper, we are interested in detecting ionization bubbles around quasars using their kSZ signature (Acharya & Majumdar 2023) (see next section for more details). Since the spectral signature of kSZ is a blackbody, one can not use the kSZ spectral signature of these bubbles to distinguish them from primary CMB anisotropy as well as kSZ due to reionization and galaxy clusters. As we are going to show in subsequent sections, the CMB and cosmological kSZ signatures will be the main source of contaminant for our signal extraction. Therefore, we work on a single frequency map (≈ 150 GHz which is the peak of CMB blackbody distribution) and use only the spatial information to filter the desired signal.

3 TEMPERATURE FLUCTUATION FROM QUASAR BUBBLES

Energetic photons from quasars can ionize and heat the surrounding gas during reionization epoch (Aghanim et al. 1996). The emitted photon spectrum can be parameterized by, $L_\nu = L_0 \left(\frac{\nu}{13.6} \right)^{-\alpha}$, where L_ν is the luminosity and $\alpha = 1.5$ is our fiducial choice. One can convert the luminosity to ionizing photon emission rate, $\dot{N} = \int_{13.6}^{\infty} \left(\frac{L_\nu}{h\nu} \right) d\nu$ which is the parameter that we will be interested in. The energetic photons immediately ionize the surrounding neutral gas. However, as the distance from the quasar increases, the photon flux decreases while the number of hydrogen atoms increases within a spherical shell of a given radius. This creates an ionization bubble with a characteristic size surrounding the quasar.

The time evolution of the size of the ionized bubble is given by (Shapiro et al. 2006a; Bolton & Haehnelt 2007),

$$R(t) = R_S [1 - \exp(-t/t_{\text{rec}})]^{1/3}, \quad (3)$$

where $R_S = \left(\frac{3\dot{N}}{4\pi\alpha_H n_H^2} \right)^{1/3}$ is the Strömngren radius, $t_{\text{rec}} = 1/(\alpha_H n_H)$ is the recombination timescale and we have assumed n_H to be the mean cosmological density at a given redshift. The size of the ionization front is a function of neutral hydrogen fraction since for a partially ionized medium, the size of the ionization front is larger compared to the same in neutral medium at a given time as there are less number of neutral hydrogen to ionize.

We assume the quasars to be active for lifetime t_Q and switched off thereafter. For $t_Q \ll t_{\text{rec}}$, the expression for the size of the bubble simplifies to $R(z) = \left(\frac{3\dot{N}t_Q}{4\pi n_H(z=0)} \right)^{1/3} (1+z)^{-1}$ (Eq. 3). For a characteristic

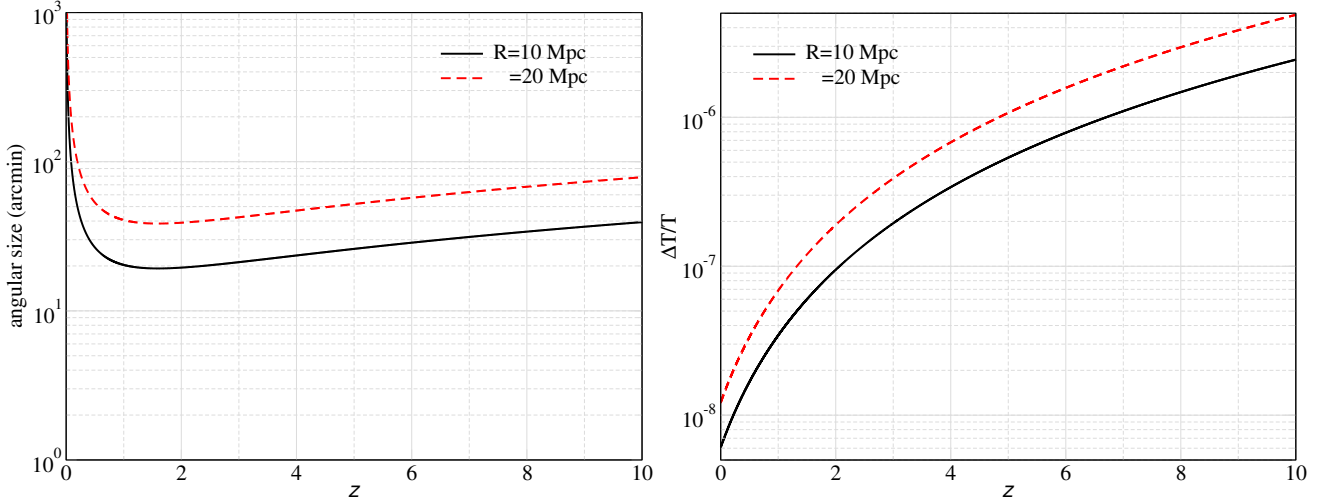


Figure 1. (a) Angular size and (b) temperature fluctuation in the direction of quasar bubble as a function of redshift for a given physical size of the bubble.

luminosity of the order $10^{46} \text{ ergs}^{-1}$ which corresponds to $\dot{N} \approx 10^{56} \text{ s}^{-1}$ (Shen et al. 2020) and $t_Q = 10^7 \text{ yr}$, the typical size is of the order $R(z) \approx 10(1+z)^{-1} \text{ Mpc}$. The typical angular scale subtended by such a bubble lies roughly between 4 – 10 arcmin for $z > 5$. The corresponding optical depth is given by $\tau = 2\sigma_T n_e R$ where σ_T is the Thomson cross-section and n_e is the background electron density at redshift z . The ionized electrons inside the bubble will give rise to both tSZ and kSZ signal, however, kinematic SZ dominates the thermal SZ by 2-3 orders of magnitude (Aghanim et al. 1996). The amplitude of kSZ signal is given by, $\frac{\delta T}{T} = \frac{v_{rms}}{\sqrt{3}c} \tau$ (Sunyaev & Zel'dovich 1980), where v_s/c is of the order 10^{-3} and can be computed from publicly available code CLASS (Blas et al. 2011). For kSZ, only the radial term contributes, which account for the numeric factor.

The temperature fluctuation for our characteristic bubbles are of the order of 10^{-7} . Since, at the arcminute scales, the temperature fluctuations due to CMB is already of the order of few μK , we are only expected to find much bigger bubbles with $\frac{\delta T}{T} \gtrsim \text{few } \mu\text{K}$. Therefore, we choose our fiducial quasar parameters to be in the range of $\dot{N} \approx 10^{58} \text{ s}^{-1}$ and $t_Q = 10^7 - 10^8 \text{ yr}$. In Fig. 1, we plot the angular size and temperature fluctuation of quasar bubble as a function of redshift for physical sizes consistent with our fiducial choice of parameters during reionization epoch ($z \sim 8$). We find that $\frac{\Delta T}{T} \approx 2 - 3 \times 10^{-6}$ with angular size $\approx 40 \text{ arcmin}$. Therefore, in this paper, we choose the fiducial amplitude of temperature fluctuation and angular size to be $6\mu\text{K}$ and 40 arcmin respectively.

The kSZ spatial template of a single quasar bubble is determined by the free electron density profile around the quasar. Detailed radiative transfer calculations (Chen & Gnedin 2021; Acharya & Majumdar 2023) show that the density profile is a box function with sharp edges. Assuming the electron number density is constant within the bubble, the observed angular dependence of the path through the bubble is proportional to $\sqrt{\theta_0^2 - \theta^2}$, where θ_0 is the angular width of the object subtended on the sky for an observer. The ionization front of quasars can expand at relativistic speeds which distorts the bubbles, making them appear anisotropic to the observer since their measured sizes along the line of sight and transverse to it will have different observed values due to relativistic time delay (Wyithe & Loeb 2004; Shapiro et al. 2006b; Yu 2005; Majumdar et al. 2011, 2012). The size of the bubble in the transverse direction would appear to be smaller than the longitudinal direction due to finite light

travel time of R/c (where R is the size of bubble) compared to the age of the quasar t_Q . Thus, the apparent transverse size R_T of the bubble is a function of time $t = t_Q - \frac{R}{c}$, whereas the longitudinal size R_L depends upon for $t = t_Q$. In principle, the two length scales can be detected by measuring its angular structure on the CMB sky and amplitude of temperature fluctuations respectively (Acharya & Majumdar 2023), however, they suffer from degeneracies as we don't have the redshift information from just CMB map. Therefore, we need to cross-correlate the CMB maps with 21cm or Lyman-alpha maps to break these degeneracies. More discussions on this topic is deferred to Sec. 8.

4 BRIEF DESCRIPTION OF MAPS AND SIMULATION

To detect quasar bubble on CMB sky using matched filters, we use simulations of CMB along with realistic foregrounds. We work in $10^\circ \times 10^\circ$ patches of the CMB Sky with 0.5 arcmin resolution, motivated by the design of CMB-HD (Sehgal et al. 2019) experiment. To simulate unlensed CMB, we use the powerspectrum obtained from CAMB¹ (Lewis & Challinor 2011). For instrumental noise, we use the specification of CMB-HD, which is 0.5 μK -arcmin. To create the lensed CMB, we first generate a Gaussian random CMB Lensing potential map using CAMB. This enables us to calculate the gravitational potential which deflect the CMB photons along the way. We apply this resulting deflections upon our Unlensed CMB Map to get the Lensed CMB.

We use the results of Sehgal et al. (2010) (hereafter, S10) for realistic simulations of microwave sky. These are realistic, full-sky, 0.5 arcmin resolution simulations of the microwave sky. The simulations include full-sky maps of the thermal SZ (tSZ), kinematic SZ (kSZ), radio galaxies, infrared galaxies, galactic Dust. The tSZ signal arises when CMB photons scattered by hot electrons via inverse Compton scattering while passing through galaxy clusters and groups. Moving electrons within these structures give rise to kSZ signal due to Doppler boosting. A second contribution to this kSZ signal is due to ionized bubbles at reionization epoch when structures start to form. The quasar bubbles that we consider here contribute to this but the reionization epoch is expected to be driven

¹ https://lambda.gsfc.nasa.gov/toolbox/camb_online.html

by galaxies and quasars are expected to be sub-dominant (Acharya & Majumdar 2023). The star forming dust regions absorb ultraviolet radiation and emit infrared radiation. Similarly, the radio point sources are the active galactic nuclei (AGNs) which includes galaxies like the Milky Way, and supernovae explosions. These sources produce synchrotron radiation due to the relativistic motion of high energy electrons in the strong magnetic fields close to supernovae and galaxies, which is then detected at radio wavelengths. There is also the thermal emission from the Galactic dust, i.e., the dust from the Milky way. In this paper, we only account for extra-galactic foregrounds. All of these maps are available in frequencies 30, 90, 148, 219, 277, 350 GHz, in the HEALPix² (Górski et al. 2005) format, with $N_{\text{side}} = 8192$. We cut out $10^\circ \times 10^\circ$ patches from the 148 GHz maps, and project them on a flat sky grid with 0.5 arcmin resolution.

4.1 Foreground subtraction

We plot the power spectra of CMB and the foregrounds in the left panel of Fig. 2. In order to detect sources at the level of few μK , the dominant foregrounds need to be removed to sufficient level. To do this, we replicate the process outlined in Han & Sehgal (2022) for foreground-reduction, with some modifications in case of the tSZ map. For IR and radio point sources, we remove the sources which will be detected at 5σ level. Equivalently, for IR map, we find pixels with fluxes above 0.03 mJy in the 148 GHz and set them to the mean value of the remaining pixels (which includes only pixels with fluxes lesser than 0.03 mJy). Due to uncertainty of these sources being extrapolated from the 280 GHz maps, we risk mis-subtracting the sources between 0.03 mJy to 0.2 mJy. Therefore, we multiply these pixels by random numbers chosen from $\mathcal{U}[-0.05, 0.05]$ (to simulate 5% uncertainty due to these sources being extrapolated from the 280 GHz maps) and the resulting products are added back to their respective pixel locations. To remove the radio sources, we mask all pixels with values corresponding to a flux equal to or greater than 0.04 mJy.

In case of the thermal SZ sources, we use the halo catalog of Sehgal et al. (2010) to mask out objects detected at 5σ level. This redshift dependent mass threshold was computed for CMB-HD experiment recently (Fig. 3, Raghunathan et al. 2022). For tSZ clusters with mass greater than this threshold, we replace them with 5 arcmin and 10 arcmin radius holes, for clusters with $z < 0.5$ and ($z > 0.5$, respectively). We then fill these holes with the mean of the pixel values of the remaining (unmasked) region to reduce the discontinuity in the region caused by the holes. We use the same mask for kSZ since these same object produce kSZ signal themselves. Since S10 does not provide separate kSZ maps from just galaxy clusters and from reionization epoch, unfortunately, this procedure masks out some of the potential contribution from reionization kSZ. Ignoring the kSZ contribution from galaxy clusters and simulating reionization kSZ using its power spectrum (Fig. 3 of Sehgal et al. (2019) assuming it to be gaussian), we find similar results compared to masked full kSZ case. The power spectra of foreground-reduced maps are shown in Fig. 2 (right panel).

5 MATCHED FILTERING WITH ONLY SIMULATED CMB AND KSZ AS FOREGROUNDS

Next, we move to our main calculations of matched-filtering the simulated CMB maps with the addition of quasar bubbles. In this section, we consider only the CMB and the reionization kSZ in addition to the instrumental noise as the main contaminant for detection of the bubbles. The CMB and kSZ have the same frequency spectrum, therefore, one can not reduce their induced background noise just by spectral information and one has to resort to spatial information to distinguish them. Hence, these calculations are ideal case scenarios where it is assumed that other foregrounds with different frequency spectrum compared to kSZ can be reduced to sufficiently small level and the CMB, kSZ from reionization and galaxy clusters set a noise floor for the detection of kSZ from a single bubble.

5.1 Constant Bubble Radius

As we have already explained, we simulate unlensed and lensed CMB using power spectrum obtained from CAMB. Similarly, we simulate reionization kSZ using the power spectrum from (Figure 3, Sehgal et al. 2019) ignoring the contribution from galaxy clusters at late redshifts. We simulate a map with few ionization bubbles with radius $40'$ and amplitude of $-6\mu\text{K}$ (at the center of the bubble), and add it to the combined map of CMB and kSZ which are shown in Fig. 3. The positions and amplitudes of these bubbles are what we wish to detect after filtering. Generally, we find that the matched-filtered map for the lensed CMB case is more noisy due to more power at smaller scales or higher ℓ . Applying the matched filter in the unlensed CMB case, we are able to detect all the bubbles, although with some error in the detected amplitude. For the lensed case however, we detect 9 of the 10 bubbles. There were no false positive detections in these cases.

5.2 Varying Source Radii

Next, we create one map containing bubbles of different sizes having randomly chosen integer between 38 and 42 arcmin. We then apply five matched filters, each with template radius θ_c as $\{38', 39', 40', 41', 42'\}$. For the unlensed and lensed case, we are able to detect 6 and 5 out of the 8 bubbles that we put in, respectively. In the Unlensed CMB case, there were no spurious detections, but in the Lensed CMB case there were 6 spurious detections. The positions and recovered amplitudes of the sources from the matched filtered maps are shown as tables Table A1 and Table A2.

6 MATCHED FILTERING WITH ALL FOREGROUNDS

We now do the calculations with unlensed/lensed CMB + all other foregrounds including the instrumental noise. For the calculations within this section, we use the masked kSZ of S10. We create a bubble map, with 10 total sources, with randomly chosen integral radii between $36'$ and $44'$, and add it to the mentioned foregrounds. Then we apply filters with varying sizes θ_c to check if the filter manages to pick out the correct size of the bubble or not. We find that the matched filter response is the highest at the correct radius as seen in Figure 4 and Figure 5 for the unlensed and lensed cases respectively. However, there is some error in recovery of the true amplitude which is expected due to the foregrounds and are tabulated in Table A3 and

² <https://healpix.sourceforge.io>

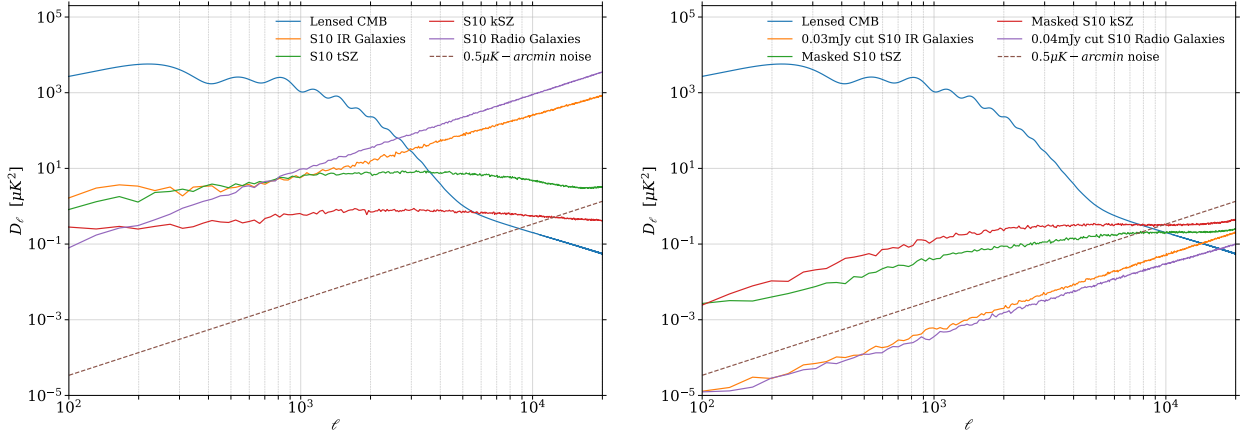


Figure 2. Power spectra of the foregrounds before (left) and after (right) the respective flux cuts and masking.

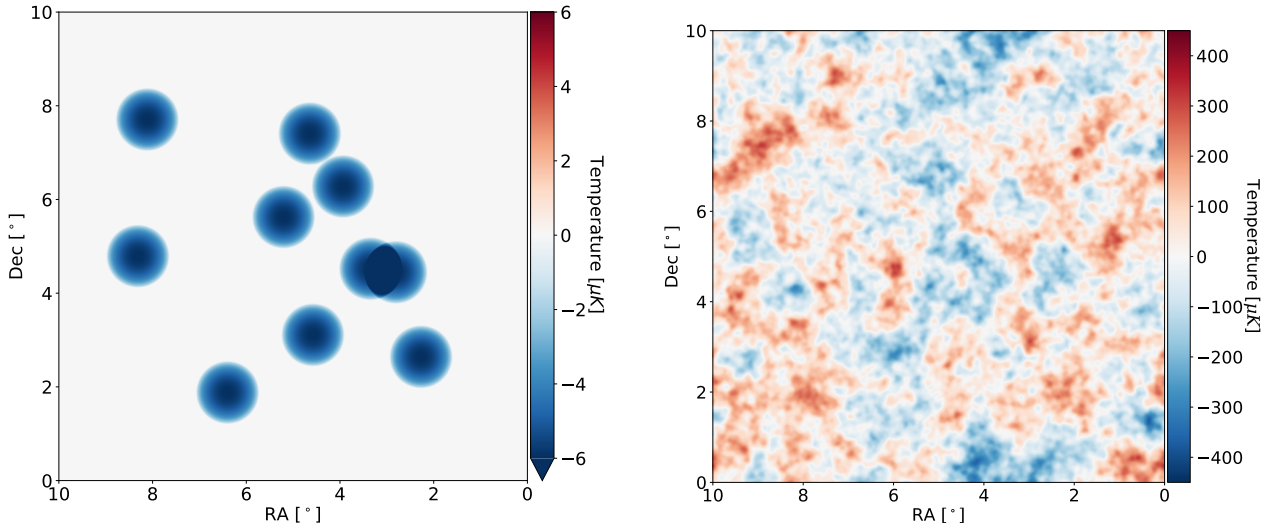


Figure 3. (Left panel) Simulated bubbles with angular size 40 arcmin and $\Delta T = -6\mu\text{K}$ at the center of bubbles, (Right) Simulated Unlensed CMB map with added simulated kSZ.

Table A4. We get 2 and 22 spurious detections in the case of unlensed and lensed case respectively. We recover 8 and 7 of the 10 sources in the unlensed and lensed cases respectively.

7 TAKING INTO ACCOUNT NON-UNIFORMITY WITHIN THE IONIZATION BUBBLES

Until now, we have assumed that the bubble profile is smooth and use the same in our choice of filter. In this section, we simulate some non-uniformity within the bubbles, to observe the effects of noisy bubble structures on the matched filtering while keeping the template filter $F_{\theta_c}(\mathbf{k})$ the same as before (same as in smoothed case). To do this, we simulate the same ionization bubble structure as in the earlier analyses, except we add gaussian noise within the structure of the bubble. We constrain this added noise to have a peak amplitude of a certain percentage of the central amplitude. This change to the bubble structure enables us to know if the template matching is robust enough to give reliable detections despite some non-uniformity in the structures to be detected. We add 30%, 10%, and 1% gaussian noise to the bubbles and redo our analysis.

We use the bubble map from Section 6 here, which means we have 10 bubbles to detect. The cumulative foreground we use here is also the same as in Section 6. The results for this are shown in Table 1 and Table 2. In both tables, mean deviation from true amplitude (%) column has items in the form of *Median* \pm *Median Absolute Deviation*. In Table 1, we see that we are able to detect the same bubbles as in smoothed case with insignificant change to the deviation from the true amplitude ($-6\mu\text{K}$) and the number of spurious detections. The only significant change we see is in the case with 30% noise within the bubbles, where we have a much larger amount of spurious detections, i.e., ~ 44 . As expected, the results worsen in the case of lensed CMB due to reasons already mentioned.

7.1 Using simulated gas profile

Next, we use the gas profile from a simulation near a dark matter halo which is shown in Fig. 6 (left panel). The halo extends to about few kpc within which the density of gas can be orders of magnitude higher than the homogenous density. However, the size of the bubble still remains the same as outside the halo, the gas density averages out to the homogenous one. The size of the bubble is of the order

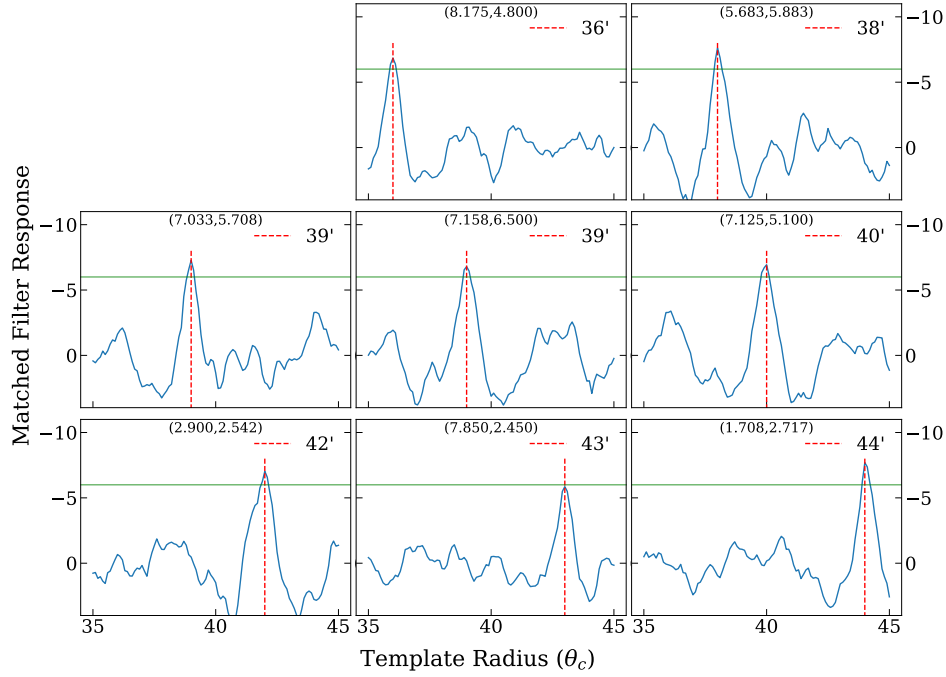


Figure 4. Matched Filter Response while varying filter radius corresponding to Table A3 (unlensed CMB+all foregrounds), with source radii (in arcmin, represented by dashed red vertical line) mentioned on the respective plots. The horizontal green line represents the true central amplitude, $-6\mu K$. The title for each subplot is in the form of (RA°, Dec°) .

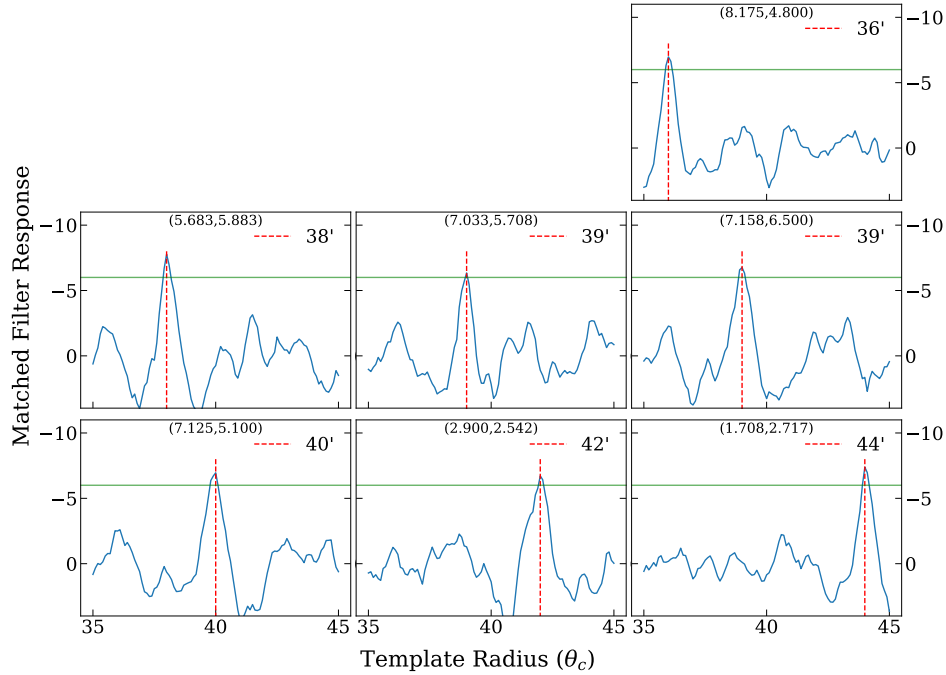


Figure 5. Matched Filter Response while varying filter radius corresponding to Table A4 (lensed CMB+all foregrounds), with source radii (in arcmin, represented by dashed red vertical line) mentioned on the respective plots. The horizontal green line represents the true central amplitude, $-6\mu K$. The title for each subplot is in the form of (RA°, Dec°) .

of 10 Mpc which is much larger than the extent of halo. Also, the resolution of our chosen CMB experiment setup is 0.5 arcmin which at $z \sim 8$ is of the order of 150 kpc. Therefore, we smooth out the density profile on such scale. In the right panel of Fig. 6, we plot the bubble profile as a function of angle for a 10 Mpc bubble at $z = 8$. At the location of halo, there is a boost in optical depth (compared

to homogenous case) due to increase in electron density at the center of halo. But at larger angles, the profile becomes similar to homogenous case but with some non-uniformity.

We add the foregrounds used in Section 6 and add the simulated bubbles to them. These are 35' radius bubbles in both cases. We take the smooth bubble profile and scale it to have a central amplitude

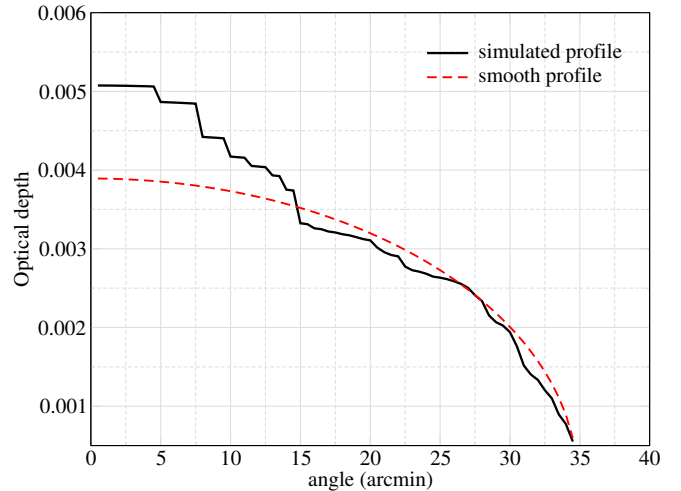
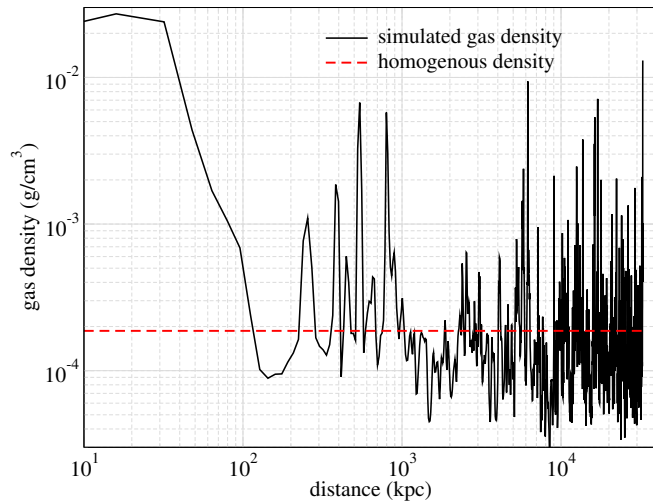


Figure 6. (a) Simulated gas profile and (b) ionized bubble profile using the simulated gas density.

Noise level in the bubbles	No. of correctly recovered sources	Median deviation from true amplitude (%)	No. of spurious detections
No noise	8	16.39 ± 3.99	2
1 %	9	16.07 ± 4.79	2
10 %	9	18.3 ± 4.8	2
30 %	8	17.24 ± 4.65	43

Table 1. Effect of non-uniformity on detected amplitude for the bubble. We use the foregrounds described in Section 6 for the the unlensed CMB case.

Noise level in the bubbles	No. of correctly recovered sources	Median deviation from true amplitude (%)	No. of spurious detections
No noise	7	15.93 ± 3.89	22
1 %	7	16.24 ± 3.91	22
10 %	8	15.54 ± 5.03	22
30 %	7	19.32 ± 3.41	44

Table 2. Same as above but for lensed case.

of $-6\mu K$, same as in earlier sections. For the comparable case with simulated gas profile, the central amplitude is $-7.822\mu K$. We apply multiple matched filters, with template radius (with the smooth bubble as template) in $\{34.0', 34.1', \dots, 35.9', 36.0'\}$, on these resulting maps, which gives us the results in Table 3. Note that since the central amplitude is $-7.822\mu K$, we note down the true amplitude as $-7.822\mu K$, and calculate the deviations using that value. Additionally, the template radius at which we get the highest SNR for all the simulated gas bubbles is $34.9'$, instead of the true radius, $35.0'$.

8 CONSTRAINING QUASAR PARAMETERS BY CROSS-CORRELATING WITH 21CM OR LYMAN-ALPHA MAPS

As noted in Sec. 3, the CMB observables of quasar ionization bubbles are the transverse angular size and amplitude of temperature fluctuation which is $\propto n_e(z)R_L$ where $n_e(z)$, R_L are the electron number density at the quasar location and the longitudinal size of the bubble respectively. The size of the bubble is a function of \dot{N} , t_Q and f_H . Therefore, just by detecting quasar bubbles in a CMB map, we can not obtain an estimate on quasar parameters such as \dot{N} and t_Q . However, the same quasar bubble can also be observed in 21cm and

Unlensed CMB + Other S10 foregrounds			
Type of bubbles	No. of correctly recovered sources	Median deviation from true amplitude (%)	No. of spurious detections
Smooth	3	29.19 ± 5.83	10
Simulated	3	13.52 ± 2.14	11
Lensed CMB + Other S10 foregrounds			
Type of bubbles	No. of correctly recovered sources	Median deviation from true amplitude (%)	No. of spurious detections
Smooth	3	32.20 ± 5.59	56
Simulated	3	10.98 ± 0.34	56

Table 3. Results for the analysis in subsection 7.1. The total number of bubbles is 6.

Lyman-alpha maps (Wyithe & Loeb 2004; Shapiro et al. 2006b; Yu 2005; Majumdar et al. 2011, 2012). Due to the tomographic nature of these observables, one can get the redshift information from these maps which is not possible from a CMB map. In addition with the knowledge of precise reionization history, we are able to get the size estimates (both R_L and R_T) from CMB observations. The combination of both R_L and R_T , should then tell us about the quasar parameters \dot{N} and t_Q as shown in Fig. 7. A bubble with higher \dot{N} expands faster, therefore, reaches the same distortion or R_T/R_L at larger t_Q . Since the size of bubble is proportional to $(\dot{N}t_Q)^{1/3}$, for such a bubble the temperature anisotropy should be higher. Therefore, measurement of amplitude of temperature anisotropy and angular size and its cross-correlation with 21cm or Lyman-alpha maps should be able to constrain the quasar intrinsic parameters.

9 CONCLUSIONS

From our results, we see that matched filtering shows promise in the detection of kSZ distortion from HII ionization bubbles. As expected, we see some problems when using non-Gaussian foregrounds (the S10 maps) that we did not encounter when using Gaussian simulations of the CMB. Methods such as multifrequency based matched multifiltering (Herranz et al. 2002) and constrained matched filters & multifilters described in Erler et al. (2019), should lead to much more consistent and accurate detections. An analogous implementa-

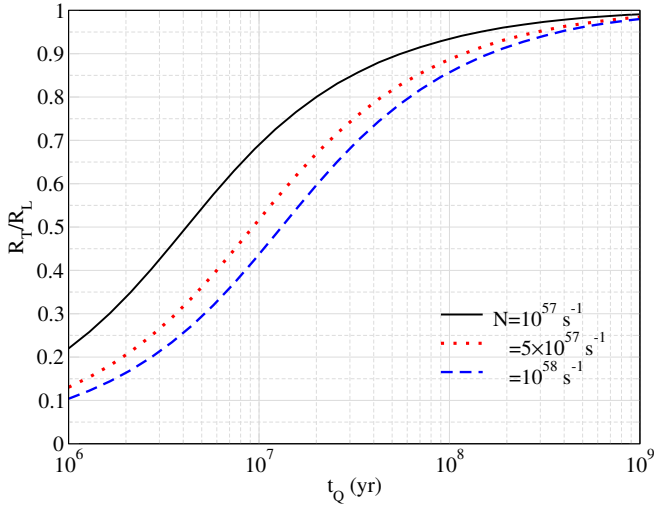


Figure 7. Distortion (R_T/R_L) as a function of quasar lifetime for different \dot{N} with $f_H = 0.5$ and $z = 8$.

tion of matched filters can be created for an all-sky maps, to avoid problems specific to projecting these maps onto a flat-sky geometry. Adapting these matched filters to spherical all-sky maps have distinct advantages (Schäfer et al. 2006). The possibility of double detections, which exists in the case of multiple flat-sky projections due to overlapping tessellation, is eliminated in the case of spherical all-sky maps. Second, any introduction of artificial non-Gaussianity due to projection, such as stretching, is circumvented when using the sphere. Finally, in case of a small patch flat-sky projection, the smallest wavenumbers are determined by the size of the map, whereas this is not the case for a sphere. Other issues come about due to lensing, which can be dealt with using CLASS_deLens³ code (Hotinli et al. 2022), which essentially delenses the CMB, solving problems caused to the matched filtering due to lensing effects.

ACKNOWLEDGEMENTS

This research made use of Photutils, an Astropy package for detection and photometry of astronomical sources (Bradley et al. 2022; Astropy Collaboration et al. 2018).

10 DATA AVAILABILITY

The data are available upon reasonable request.

REFERENCES

- Acharya S. K., Majumdar S., 2023, MNRAS
 Aghanim N., Desert F. X., Puget J. L., Gispert R., 1996, A&A, 311, 1
 Astropy Collaboration et al., 2018, AJ, 156, 123
 Blas D., Lesgourgues J., Tram T., 2011, JCAP, 2011, 034
 Bolton J. S., Haehnelt M. G., 2007, MNRAS, 374, 493
 Bradley L. et al., 2022, astropy/photutils: 1.6.0
 Chen H., Gnedin N. Y., 2021, ApJ, 911, 60
 Erler J., Ramos-Ceja M. E., Basu K., Bertoldi F., 2019, Monthly Notices of the Royal Astronomical Society, 484, 1988

- Górski K. M., Hivon E., Banday A. J., Wandelt B. D., Hansen F. K., Reinecke M., Bartelmann M., 2005, ApJ, 622, 759
 Haehnelt M. G., Tegmark M., 1996, MNRAS, 279, 545
 Han D., Sehgal N., 2022, Physical Review D, 105
 Herranz D., Sanz J. L., Hobson M. P., Barreiro R. B., Diego J. M., Martínez-González E., Lasenby A. N., 2002, Monthly Notices of the Royal Astronomical Society, 336, 1057
 Hotinli S. C., Meyers J., Trendafilova C., Green D., van Engelen A., 2022, JCAP, 2022, 020
 Lewis A., Challinor A., 2011, CAMB: Code for Anisotropies in the Microwave Background. Astrophysics Source Code Library, record ascl:1102.026
 Majumdar S., Bharadwaj S., Choudhury T. R., 2012, MNRAS, 426, 3178
 Majumdar S., Bharadwaj S., Datta K. K., Choudhury T. R., 2011, MNRAS, 413, 1409
 Melin J. B., Bartlett J. G., Delabrouille J., 2005, A&A, 429, 417
 Melin J. B., Bartlett J. G., Delabrouille J., 2006, A&A, 459, 341
 Melin, J.-B., Bartlett, J. G., Tarrío, P., Pratt, G. W., 2021, A&A, 647, A106
 Ofek E. O., Zackay B., 2018, AJ, 155, 169
 Planck Collaboration et al., 2016, A&A, 594, A27
 Planck Collaboration et al., 2014, A&A, 571, A29
 Raghunathan S. et al., 2022, The Astrophysical Journal, 926, 172
 Schäfer B. M., Pfrommer C., Hell R. M., Bartelmann M., 2006, Monthly Notices of the Royal Astronomical Society, 370, 1713
 Sehgal N., Bode P., Das S., Hernandez-Monteagudo C., Hufferberger K., Lin Y.-T., Ostriker J. P., Trac H., 2010, ApJ, 709, 920
 Sehgal et. al. N., 2019, in Bulletin of the American Astronomical Society, Vol. 51, p. 6
 Shapiro P. R., Iliev I. T., Alvarez M. A., Scannapieco E., 2006a, ApJ, 648, 922
 Shapiro P. R., Iliev I. T., Alvarez M. A., Scannapieco E., 2006b, ApJ, 648, 922
 Shen X., Hopkins P. F., Faucher-Giguère C.-A., Alexander D. M., Richards G. T., Ross N. P., Hickox R. C., 2020, MNRAS, 495, 3252
 Sunyaev R. A., Zeldovich I. B., 1980, MNRAS, 190, 413
 Vanderlinde K. et al., 2010, The Astrophysical Journal, 722, 1180
 Vio R., Andreani P., 2018, A&A, 616, A25
 Wyithe J. S. B., Loeb A., 2004, ApJ, 610, 117
 Yu Q., 2005, ApJ, 623, 683
 Zubeldia Í., Rotti A., Chluba J., Battye R., 2021, MNRAS, 507, 4852

APPENDIX A: MATCHED FILTER RESULTS

³ https://github.com/selimhotinli/class_delens

$Radius(\theta_x^\circ, \theta_y^\circ)$	MF Radius (')	Recovered Amplitude
38(5.217,4.858)	38	-6.403549
38(4.442,7.158)	38	-5.914817
39(3.275,3.742)	39	-7.799565
40(5.500,3.225)	40	-8.303618
40(2.192,2.875)	40	-7.272582
42(6.900,5.817)	42	-6.607460

Table A1. Source Detection with the Matched Filter applied on Unlensed CMB + simulated reionization kSZ + HII Ionization bubbles + instrumental noise. $(\theta_x^\circ, \theta_y^\circ)$ are the positions of the bubble sources. Actual amplitude for all sources is $-6\mu K$.

$Radius(\theta_x^\circ, \theta_y^\circ)$	MF Radius (')	Recovered Amplitude
38(5.217,4.858)	38	-6.834603
39(3.275,3.742)	39	-7.636465
40(5.500,3.225)	40	-8.511117
40(2.192,2.875)	40	-7.348668
42(6.900,5.817)	42	-6.313925

Table A2. Same as above but with lensed CMB.

$Radius(RA^\circ, Dec^\circ)$	MF Radius (')	Recovered Amplitude
36(8.1754,800)	36	-6.838021
38(5.6835,883)	38	-7.619793
39(7.0335,708)	38	-7.268827
39(7.1586,500)	39	-6.789971
40(7.1255,100)	39	-6.936532
42(2.9002,542)	40	-7.030653
43(7.8502,450)	42	-5.856849
44(1.7082,717)	43	-7.693487

Table A3. Source Detection with the Matched Filter applied on Unlensed CMB + all foregrounds including masked kSZ of S10 maps+ HII Ionization bubbles + white noise. Actual amplitude for all sources is $-6\mu K$.

$Radius(RA^\circ, Dec^\circ)$	MF Radius (')	Recovered Amplitude
36(8.175,4.800)	36	-6.975150
38(5.683,5.883)	38	-7.779363
39(7.033,5.708)	39	-6.347103
39(7.158,6.500)	39	-6.756921
40(7.125,5.100)	40	-6.955670
42(2.900,2.542)	42	-6.722138
44(1.708,2.717)	44	-7.381340

Table A4. Same as above but with lensed CMB.